Transcranial Functional Ultrasound Imaging Detects Focused Ultrasound Neuromodulation Induced Hemodynamic Changes in Mouse and Nonhuman Primate Brains *In Vivo*

Christian Aurup[1], Jonas Bendig[1], Samuel G. Blackman[1], Erica P. McCune[1], Sua Bae[1], Sergio Jimenez-Gambin[1], Robin Ji[1], and Elisa E. Konofagou[1,2]

[1]Department of Biomedical Engineering, Columbia University, New York, NY, USA

[2]Department of Radiology, Columbia University, New York, NY, USA

Correspondence to: Elisa E. Konofagou
Full address: 630 West 168th Street, New York, NY 10032, USA
E-mail: ek2191@columbia.edu

Abstract

Focused ultrasound (FUS) is an emerging noinvasive technique for neuromodulation in the central nervous system (CNS). To evaluate the effects of FUS-induced neuromodulation, many studies used behavioral changes, functional magnetic resonance imaging (fMRI) or electroencephalography (EEG). However, behavioral readouts are often not easily mapped to specific brain activity, EEG has low spatial resolution limited to the surface of the brain and fMRI requires a large importable scanner that limits additional readouts and manipulations. In this context, functional ultrasound imaging (fUSI) holds promise to directly monitor the effects of FUS neuromodulation with high spatiotemporal resolution in a large field of view, with a comparatively simple and flexible setup. fUSI uses ultrafast Power Doppler Imaging (PDI) to measure changes in cerebral blood volume, which correlates well with neuronal activity and local field potentials. We designed a setup that aligns a FUS transducer with a linear array to allow immediate subsequent monitoring of the hemodynamic response with fUSI during and after FUS neuromodulation. We established a positive correlation between FUS pressure and the size of the activated area, as well as changes in cerebral blood volume (CBV) and found that unilateral sonications produce bilateral hemodynamic changes with ipsilateral accentuation in mice. We further demonstrated the ability to perform fully noninvasive, transcranial FUS-fUSI in nonhuman primates for the first time by using a lower-frequency transducer configuration.

Keywords: Focused Ultrasound, Neuromodulation, Functional Ultrasound, Nonhuman primate

Introduction

Focused ultrasound (FUS) has shown the ability to noninvasively modulate neuronal activity in the central nervous system of different animal species as well humans[1–9]. In contrast to established neuromodulatory techniques like deep brain stimulation, transcranial magnetic stimulation or transcranial (direct) current simulation, FUS combines a favorable safety profile with the ability to target deep brain structures with spatial resolution in the millimeter (e.g. humans) or sub-millimeter range (e.g. rodents)[9,10]. In a previous study, we introduced a robust technique for performing FUS neuromodulation in mice *in vivo*[11]. However, *in silico* ultrasound simulations indicated that transcranial pressure field patterns are difficult to predict and that intracranial acoustic reverberations can generate additional pressure peaks sufficient to activate the brain outside of the intended focal target. More direct measurements of evoked brain activity are therefore needed to fully assess the acute and long-term effects of FUS in the targeted area as well as connected brain regions.

Electroencephalography (EEG)[12,13] and functional magnetic resonance imaging (fMRI)[14,15] are the most common techniques for studying neuronal activity in animal models and humans. However, EEG is not capable of directly localizing activity in deep brain regions and fMRI requires long imaging sessions in a spatially confined MRI scanner with high capital costs[16–18]. In contrast, functional ultrasound imaging (fUSI) is an emerging imaging technique[19–21] that allows monitoring of stimulus-evoked activity and functional connectivity in the whole brain with a comparatively small ultrasound array[22–25]. fUSI uses ultrafast Power Doppler Imaging (PDI) to measure changes in cerebral blood volume while suppressing signals from the surrounding tissue through the implementation of advanced spatiotemporal filtering techniques such as singular value decomposition (SVD)[26,27]. Analogous to fMRI, fUSI leverages neurovascular coupling and has been shown to correlate well with neuronal activity and local field potentials[28,29]. The spatial resolution is similar to that of fMRI[30] but it attains greater temporal resolution[16].

The principal challenge in applying transcranial fUSI to the brain is the substantial acoustic attenuation induced by the skull. Consequently, most implementations of fUSI to date have relied on removal or thinning of the skull bone[18]. Previous work by our group and others has demonstrated transcranial applications of fUSI for detecting hemodynamic changes in the mouse brain[23,31–33], allowing for a fully noninvasive ultrasound-based functional brain imaging technique.

Although recent studies have demonstrated implementations of fUSI in Nonhuman primates (NHPs)[34–37], the substantially thicker skull has, to date, precluded transcranial applications of the technique. Achieving transcranial fUSI in combination with FUS could allow noninvasive neuromodulation with simultaneous monitoring of neuromodulatory effects in a large field of view.

In this study, we developed a simultaneous FUS and power Doppler imaging transducer configuration to assess the immediate and short-term effects of FUS neuromodulation with transcranial fUSI. We demonstrate that the size of the activated area is positively correlated with the magnitude of the applied pressure and that unilateral sonications produce bilateral hemodynamic changes with ipsilateral bias in mice. We further tested the feasibility of using a lower-frequency transducer configuration in NHP *in vivo* and demonstrated the ability to perform fully noninvasive, transcranial FUS-fUSI in a thicker-skulled animal model for the first time.

Methods

Mice preparation

Young male wild-type mice between 8 to 12 weeks of age (C57BL/6, n = 22) were used for transcranial experiments in this study. To assess possible effects of the skull, a subgroup of mice between 8 to 20 weeks of age (C57BL/6, n = 5) was implanted with a chronic cranial window covered by a polymethyl pentene membrane as described by Brunner et al[20]. Mice implanted with a cranial window were allowed to rest for 2 weeks before experiments were performed. Anesthesia was induced with isoflurane (1-3%) and supplementary oxygen (0.8 L/min). The absence of a pedal reflex confirmed induction and isoflurane was then decreased and adjusted between 0.5-1% to maintain light anesthesia without producing gasping from low oxygenation, which can increase motion artifacts during imaging sessions. The subject's head was fixed by a stereotactic frame (Model 900, David Kopf Instruments, Tujunga, CA, USA) using ear and bite bars to immobilize the head. Elastic bands were then placed around the ear bars and passed over the subject's body to mitigate motion artifacts from respiration. The animal's head was shaved and depilatory cream was used to remove all remaining fur to optimize acoustic coupling with acoustic gel placed on the subject's head. A piece of polyethylene was cut with a hole the size of the head and fastened

to the ear bars. Mice with cranial windows were fixed with a 3D-printed holder that connected to the implanted headpost and acoustic gel was placed on the membrane covering the cranial window.

A data acquisition (DAQ) system (MP150, Biopac Systems Inc, Goleta, CA) was used to acquire pulse-oximetry signals (MouseOx+, Starr Life Sciences, Oakmont, PA, USA) recorded from a sensor placed on the shaved thigh. The pulse-oximeter was used in conjunction with intermittent toe pinches to monitor the depth of anesthesia. The ideal depth of anesthesia during experiments corresponded with heart rates above 400 bpm and an unresponsive pedal reflex. A diagram showing the configuration of experimental equipment is provided in Figure 1. The full animal preparation for mice and NHP is provided in Figure 1.

NHP Preparation

FUS neuromodulation with fUSI was performed across multiple experimental sessions in 2 male Rhesus macaques (age: 130 months and 133 months). The animals were sedated, intubated, and an intravenous catheter was placed in the saphenous vein to allow for administration of fluids, microbubbles, and magnetic resonance (MR) contrast agents. Anesthesia monitoring was provided by on-site veterinary staff. The animal's head was immobilized in a stereotactic frame and the scalp was shaved and depilatory cream used to fully remove any remaining fur before applying acoustic coupling gel. FUS neuromodulation experiments were immediately followed by a FUS blood-brain barrier opening (BBBO) session at the same location to validate targeting via Gadolinium uptake in a subsequent contrast-enhanced MRI scan as described previously[38].

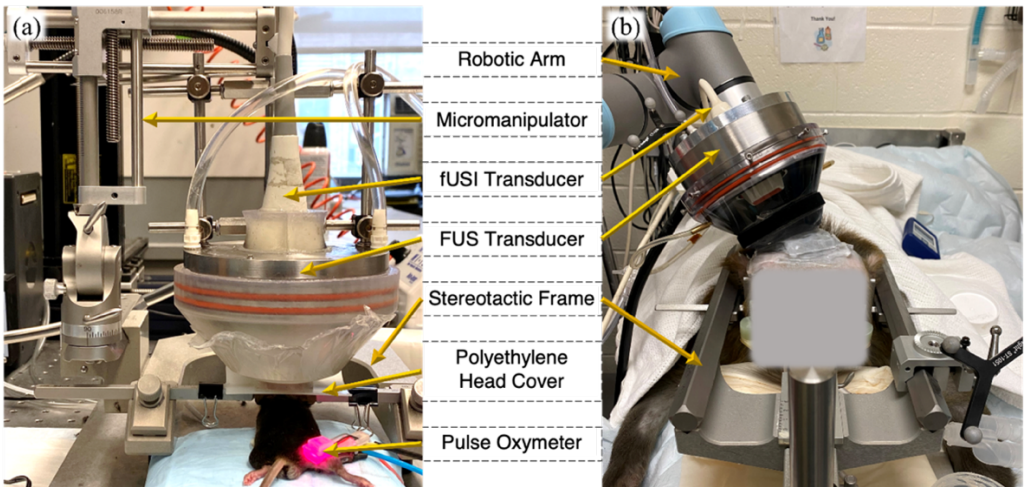

Figure 1. Experimental setups for mice (**a**) and NHP (**b**). The relevant shared and differing components between both setups are labeled.

FUS Neuromodulation in Mice and NHP

A single-element spherical segment annular focused ultrasound transducer with confocally aligned ultrasound imaging arrays were used in both mice and NHP in this study (Table 1). Each transducer had an acoustic coupling cone attached to the transducer face with an acoustically transparent membrane (Tegaderm, 3M Company, Maplewood, MN, USA) placed over its opening. The sealed coupling chamber was then filled with deionized water and degassed using a degassing system (WDS105+; Sonic Concepts, Bothell, WA, USA). FUS transducers were calibrated in a degassed water tank using a hydrophone (HGL0200, Onda Corporation, Sunnyvale, CA, USA) and ex vivo skulls for estimating attenuation and reporting derated pressures. FUS sequences were driven by function generators and RF amplifiers. The specifications of the different equipment used and related acoustic parameters in the mouse and NHP experiments are provided in Table 1.

Table 1. FUS and fUSI equipment and acoustic parameters.

	Mice	Nonhuman Primates
	FUS	
Transducer	H-204 (Sonic Concepts Inc, Bothell, WA, USA); Focal Size (-6 dB): 0.8 mm (lateral), 8 mm (axial) H-215 (Sonic Concepts Inc, Bothell, WA, USA); Focal Size (-6 dB): 0.3 mm (lateral), 2 mm (axial)	H-231 (Sonic Concepts Inc, Bothell, WA, USA) Focal Size (-6 dB): 6 mm (lateral), 49 mm (axial)
RF Amplifier	325LA, Electronics Innovation Ltd., Rochester, NY, USA	A075 (Electronics Innovation Ltd., Rochester, NY, USA)
Acoustic Parameters	Carrier Frequency: H-204: 1.68 MHz (3rd Harmonic) H-215: 4 MHz Amplitude Modulation Freq: 1 kHz Burst Duration: 150 ms Sonication Frequency: H-204: 1 Hz H-215: 2 Hz Peak Negative Pressures: 0.8-2.6 MPa (Derated, transcranial, H204) 0.7-2.8 MPa (Cranial window, H204) 1.4-3.6 MPa (Cranial window, H215)	Center Frequency: 0.25 MHz (Fundamental) Pulse Repetition Frequency: 1 kHz Duty Cycle: 50% Burst Duration: 300 ms Sonication Frequency: ~0.5 Hz Peak Negative Pressure: 1.2 MPa (Derated)

	fUSI	
Transducer	L22-14vXLF (Vermon S.A., Tours, France)	P4-2 (ATL/Philips, Andover, MA,USA)
Acoustic Parameters	Center frequency: 15.0 MHz Compounded Plane Wave Imaging Plane Angles: 5 (-6° to 6°) Compounded Image Rate: 500 Hz Compounded Images in PDI: 200 (transcranially) 70 (craniotomized)	Center frequency: 3.0 MHz Compounded Diverging Wave Imaging Virtual Sources (VS): 5 VS Depth/Interval: -50mm/3mm Compounded Image Rate: 800 Hz Compounded Images in PDI: 500
Filtering	Singular Value Decomposition: 10% of singular values removed High-Pass Filter: Butterworth (2nd order), 8-Hz cutoff frequency	Singular Value Decomposition: 10% of singular values removed High-Pass Filter: Butterworth (4th order), 4.5-Hz cutoff frequency

In mice, amplitude-modulated (AM) sequences were implemented to mitigate confounding auditory effects associated with using pulsed ultrasound in small animal studies[39,40]. It is expected that the smooth envelope in AM ultrasound is less likely than the square envelope in pulsed ultrasound to produce auditory confounds[41]. A comparison of AM and the pulsing scheme used in NHPs is depicted in Supplementary Figure 1. The FUS transducer was attached to the stereotactic frame using a stereotactic micromanipulator (David Kopf Instruments, Tujunga, CA, USA). A block design was implemented consisting of a 60-second baseline imaging block followed by four 30-second FUS blocks with intervals randomized between 60 and 90 seconds. During the FUS blocks, the function generator output was triggered by the imaging system directly after image acquisition to avoid any interference between the FUS and fUSI. In NHP, pulsed sequences were utilized in testing the feasibility of the technique. The block design also differed slightly from the mouse experiments. Single trials were conducted consisting of a 20-frame (~40 seconds) baseline block, a 10-frame (~20 seconds) FUS block, and a 20-frame (~40 seconds) post-stimulus block. At least 6 stimulus trials were performed at each target and fUSI datasets were averaged across trials. The imaging and FUS block designs for mice and NHP are provided in Figure 2.

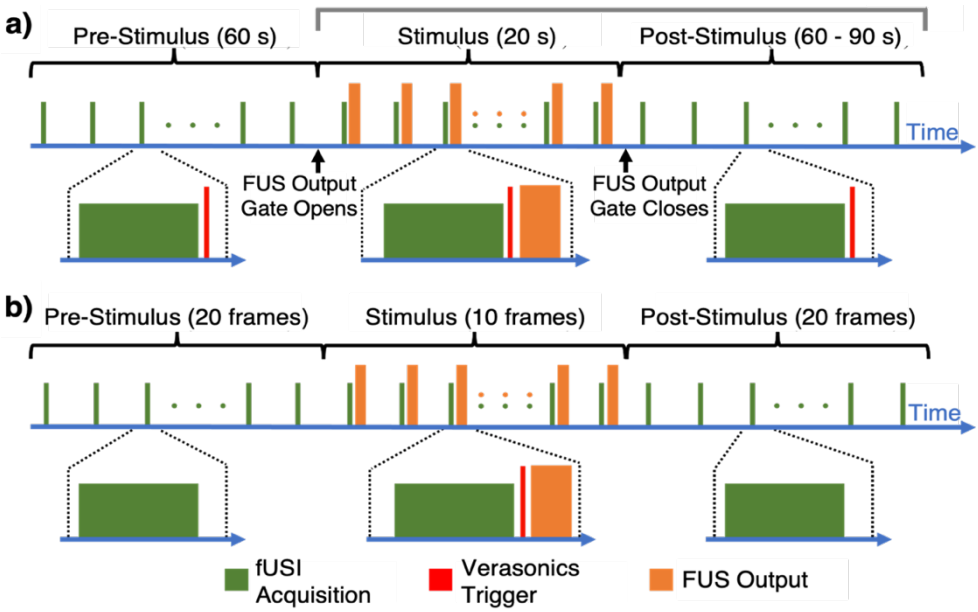

Figure 2. fUSI and FUS stimulus block designs for singular trials. The stimulus and post-stimulus periods in mice (**a**) are looped four times while not looped in NHP (**b**). FUS is triggered by the fUSI system in both setups. In (**a**), every fUSI acquisition transmits a trigger pulse and FUS output is controlled by a programmed gate. In (**b**), fUSI only transmits triggers during the stimulus phase.

Functional Ultrasound Imaging (fUSI)

fUSI was implemented to detect and characterize stimulus-evoked hemodynamic changes in mouse and NHP brains. This study utilized linear array ultrasound imaging transducers confocally aligned within the annular opening of its paired FUS transducer. Imaging sequences were generated using a programmable research ultrasound system (Vantage 256, Verasonics, Kirkland, WA) to perform ultrafast compounded plane wave imaging. fUSI was performed by acquiring a time series of coronal power Doppler images (PDI). The imaging parameters utilized in the mouse and NHP experiments are provided in Table 1. A single compounded image was generated by averaging delay-and-sum reconstructed ultrasound images acquired from multiple plane wave transmits in mice and diverging wave transmits in NHP. A PDI was generated by first applying a high-pass filter to a stack of compounded images followed by spatiotemporal filtering using singular value decomposition (SVD)[26,27]. SVD filtering cannot remove the influence of large motion artifacts, so outlier frames were removed whose mean image value was three standard deviations above the mean image value of the remaining image set. The pixel intensity data, representing cerebral blood volume (CBV), was averaged across the four stimuli prior to performing the statistical analysis. The image processing steps are outlined in Figure 3.

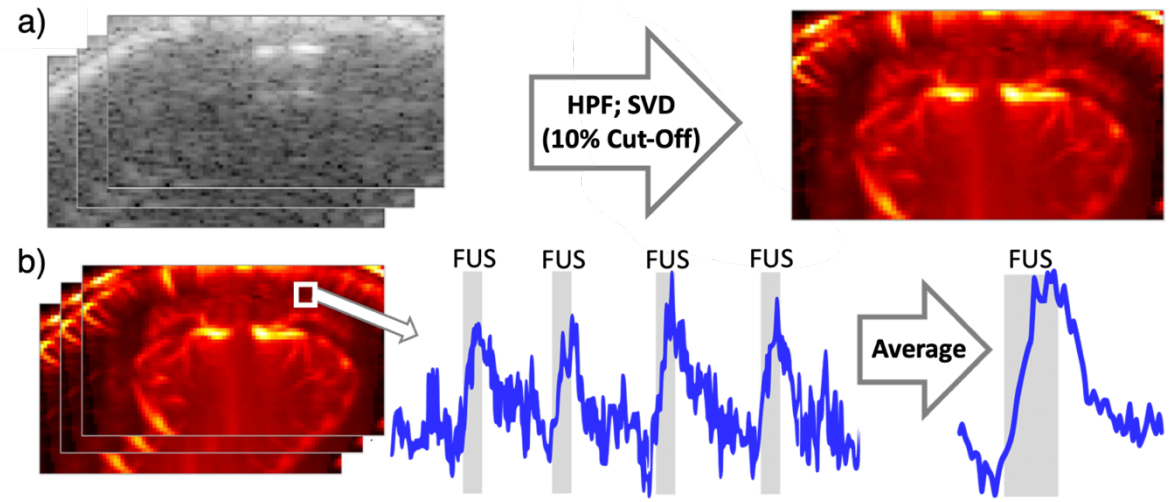

Figure 3. fUSI image processing steps and averaging. (**a**) Power Doppler images (PDI) were generated from stacks of compounded images. A high-pass filter (HPF) was applied prior to performing singular value decomposition (SVD). An eigenvalue cutoff of 10 % was chosen to filter out the tissue clutter signal. These datasets were then recomposed using the same eigenvalue cutoff, yielding a time series of PDI. (**b**) PDI pixel intensity time series were averaged across focused ultrasound (FUS) stimuli for each trial before performing statistical analysis.

Neuronavigation and Targeting

The confocal FUS-fUSI transducer system was lowered into the acoustic gel on the scalp, ensuring that no bubbles were trapped along the beam path. B-Mode imaging was used to verify adequate acoustic coupling (Figure 4). In mice, the transducer system was attached to a stereotactic micromanipulator. Targeting was performed by first landmarking the interaural line using B-mode imaging to locate highly reflective metal syringe tips temporarily placed on the stereotactic ear bars (i.e. interaural line). The syringe tips were then removed, taking extra care not to leave trapped air bubbles that could result in signal loss or artifacts. Neuronavigation could then be performed by manually translating the transducer system in the anteroposterior or mediolateral (ML) directions according to a reference atlas[42] using the micromanipulator. In animals with cranial windows, targeting was performed by using the anterior border of the cranial window (Bregma +2 in the anterioposterior direction) as a reference point. The imaging plane was located at -1.6 mm to -2.0 mm from Bregma in the anterioposterior direction. Sonications were performed along the midline (± 0 mm ML) or at ± 2 mm ML to investigate possible lateralization.

In NHP, the FUS-fUSI transducer system was fixed to a robotic arm (UR5e, Universal Robots, Denmark) that allowed for precision targeting anywhere in the brain. Transducer positioning was performed using a neuronavigation system (Brainsight; Rogue Research, Montreal, QC, Canada) that allowed for preselection of brain targets and planning of trajectories. This neuronavigation procedure has been described previously[38,43,44]. The selection of targets and determination of trajectories were performed manually using previously acquired anatomical MRI scans uploaded to the neuronavigation software (Figure 4). The robotic arm allowed for highly precise transducer positioning with respect to the planned target and trajectory. Nevertheless, the target and trajectory immediately prior to sonications was saved and used to predict transcranial pressure fields in simulations using k-Wave[45]. Simulations allowed for the spatial comparison of predicted pressure fields with fUSI data.

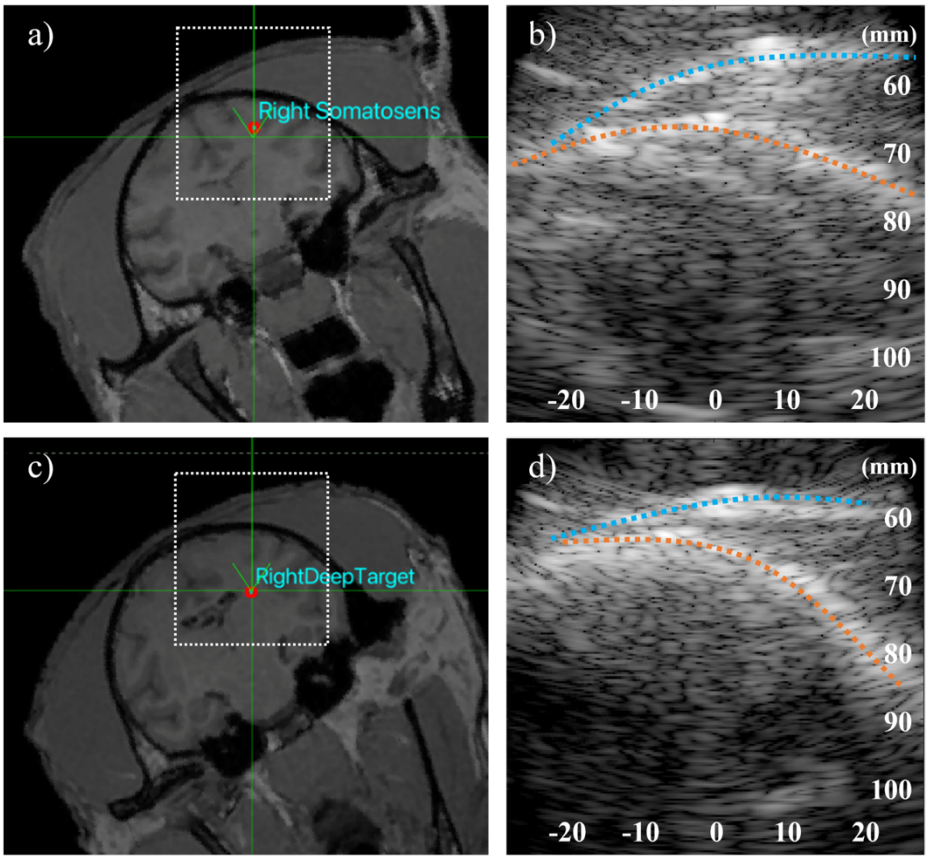

Figure 4. Planned FUS targets and associated B-Mode images. Targeting was performed with the Brainsight neuronavigation system **(a** and **c)** and B-Mode images were used to ensure proper acoustic coupling and alignment (**b** and **d**). Both modalities are shown for the first (**a** and **b**) and the second subject (**c** and **d**). The skin surface (blue dotted line) and skull (orange dotted line) are marked on each B-Mode image.

Correlation Analysis

Statistical analyses were performed to identify pixels exhibiting intensity time courses that were significantly correlated with applied stimulus patterns in a manner as in our previous study[31]. The binary stimulus vector (i.e. FUS ON vs FUS OFF) was convolved with a modified hemodynamic response function (HRF)[20] to generate a more physiologically relevant HRF regressor for computing correlation coefficients. Using the binary vector as a regressor yields significance; however, using a physiologically relevant regressor is optimal because changes in CBV are not instantaneous. Pixel-wise Spearman correlation coefficients were computed between the regressor and PDI time series. Pixels with significantly correlated ($p < 0.01$) CBV changes were identified in each session and used to create binary maps. Small areas of connected pixels were removed from the binary maps to isolate the spatially dominant effects (<0.05 mm^2 in mice; < 15 mm^2 in NHP). The computed correlation values were then remapped using the binary maps to be overlaid onto mean PDI, B-mode, or anatomical MRI. The main steps are summarized in Figure 5.

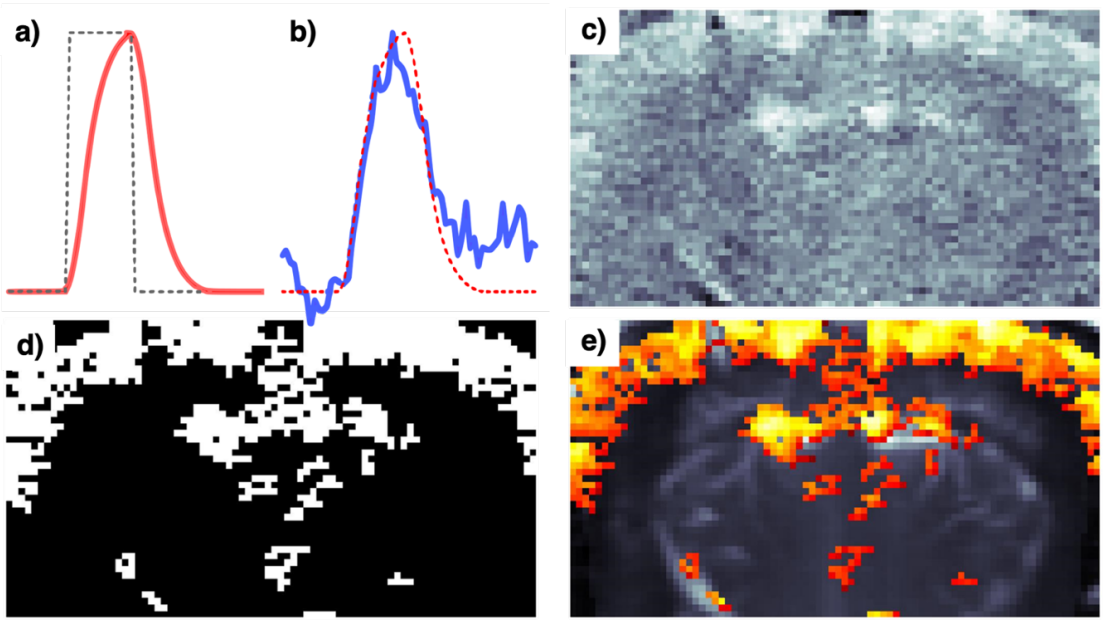

Figure 5. Correlation analysis of pixel intensity over time with the applied stimulus pattern. (**a**) The binary stimulus vector (dotted line) was convolved with a modified hemodynamic response function (HRF) to generate a physiologically relevant regressor (red solid line) used in computing correlation coefficients according to Brunner et al. 2021. **(b)** The regressor (dotted red line) is shown relative example stimulus-averaged pixel intensity time series (blue solid line). **(c)** Maps of Spearman correlation coefficients were computed between stimulus-averaged pixel intensity time series and the regressor for each dataset. **(d)** Significantly correlated pixels ($p<0.01$) were identified and small pixel groups were removed to create binary activity maps. **(e)** Correlation coefficients were remapped and overlaid onto averaged PDI.

Results

Mice

The ultrasound imaging sequence implemented in this study was able to successfully transcranially image the mouse brain *in vivo*. The immobilization techniques implemented adequately mitigated motion artifacts such that fewer than 5% of image frames were removed as outliers in all image sets. Experiments were performed to determine whether FUS induces hemodynamic changes in the brain. A total of 22 sham trials were conducted across 6 mice. Sham trials performed with the amplifier powered off showed no significant activation. However, FUS routinely produced widespread hemodynamic responses in all subjects. Activity was typically observed both within the focal region and across both hemispheres of the cortex. Example sham results for two subjects receiving both sham (0 MPa) and FUS (1.7 MPa) conditions are provided in Figure 6. The FUS condition induced significantly greater activation area size than the sham groups ($p < 0.001$, Wilcoxon matched-pairs signed rank test).

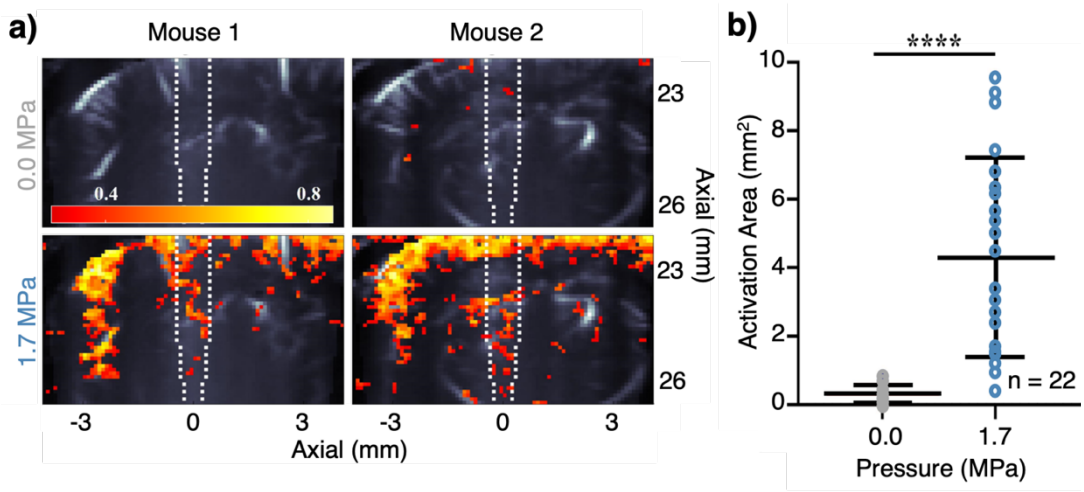

Figure 6. Activation in FUS and sham trials. **(a)** Activity maps of Spearman correlation coefficients for two subjects receiving both sham and FUS conditions are overlaid onto PDI. The predicted acoustic focus assessed during transducer calibration is overlaid with a white dotted line. **(b)** Wilcoxon matched-pairs signed rank test revealed a significantly greater activation area in the FUS group. (****$p < 0.001$)

Further FUS experiments were performed to determine whether response patterns demonstrate a dependence on the applied acoustic pressure. 4 subjects were sonicated with 3 different FUS pressures in randomized order for a total of 9 trials (n = 2 trials for 3 subjects and n = 3 trials for 1 subject). A sample of each pressure condition for 3 subjects is provided in Figure 7.

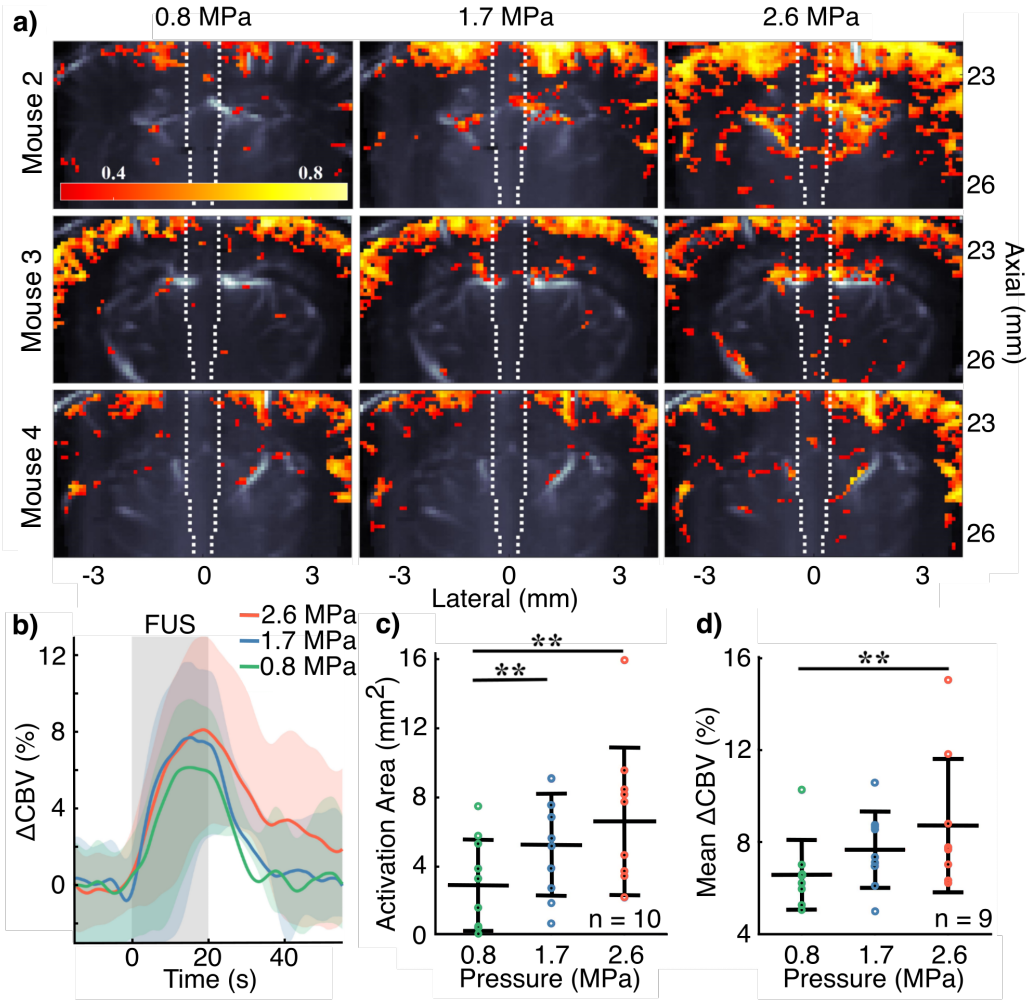

Figure 7. Higher pressures of transcranial FUS induce greater activation. **(a)** Activity maps for three subjects receiving 0.8, 1.7, and 2.6 MPa FUS. Spearman coefficients of significantly correlated pixels and the predicted acoustic focus (white) assessed during transducer calibration are overlaid onto PDI. The color bar represents Spearman correlation values. **(b)** Mean CBV changes (solid) and standard deviations (shaded) for all jointly significantly correlated pixels across all trials. Multiple Wilcoxon matched-pairs signed rank tests revealed significantly greater **(c)** activation area and **(d)** CBV change as pressure increased. (**$p < 0.01$). Data is depicted as individual observations (circles) with mean (central line) and standard deviations (whiskers).

A Friedman test revealed a significant difference between the pressure groups ($p < 0.001$). The size of the activation area was observed to increase significantly with the applied FUS pressure from 0.8 to 2.6 MPa. Wilcoxon matched-pairs signed rank tests showed that the 1.7 and 2.6 MPa group both produced greater activation areas than the 0.8 MPa group ($p < 0.01$). The 2.6 MPa group compared with the 1.7 MPa did not rise to significance; however, linear regression showed a significant positive trend ($p < 0.05$) in activation area size with increasing pressure. Mean

changes in CBV were calculated by averaging significantly correlated pixels that were common to each of the three pressure conditions for each individual trial. Selecting pixels that were jointly significant across pressure conditions was intended to reduce bias in datasets with stronger correlation and more significant pixels. In one subject, the 0.8 MPa condition did not yield any significance and was therefore omitted from the CBV analysis. Wilcoxon matched-pairs signed rank tests showed that the 2.6 MPa group produced a greater mean change in CBV than the 0.8 MPa group ($p < 0.01$).

To investigate the effects of the skull on the response patterns, FUS was delivered with different pressures in 5 mice implanted with cranial windows. We further evaluated possible effects of frequency and focal size, by using a 4 MHz transducer to deliver FUS with comparable pressures. Like the transcranial condition, there were significant differences between the pressure groups for both tested frequencies (Friedman test, 1.68 MHz: $p = 0.0014$, 4.0 MHz: $p = 0.0002$). A Dunn's test corrected for multiple comparisons was performed as a post-hoc analysis to account for the small group size. We found significantly larger activated areas in 2.8 MPa FUS compared to the lower pressures of 0.7 MPa ($p = 0.0443$), 1.1 MPa ($p = 0.0070$) or 1.4 MPa ($p = 0.0208$) in the 1.68 MHz condition (Figure 8b). Similarly, with 4 MHz FUS the activated area with pressures $\geq$ 3.0 MPa was significantly larger compared to 1.4 MPa (Dunn's Test, 3 MPa: $p = 0.00175$, 3.3 MPa: $p = 0.0437$, 3.6 MPa: $p = 0.0175$, Figure 8a). Clear trends for an increase in activated areas start at pressures of 2.1 MPa in the 1.68 MHz condition and at 2.3 MPa in the 4 MHz condition (Figure 8b/c). Compared to transcranial FUS there was no activation in lower pressure conditions (i.e. 0.8 MPa and 1.7 MPa) and correlation coefficients of significantly activated areas were lower. Especially in lower pressures, cortical activation was less pronounced in mice with cranial windows, while subcortical responses appeared enhanced (Figure 8).

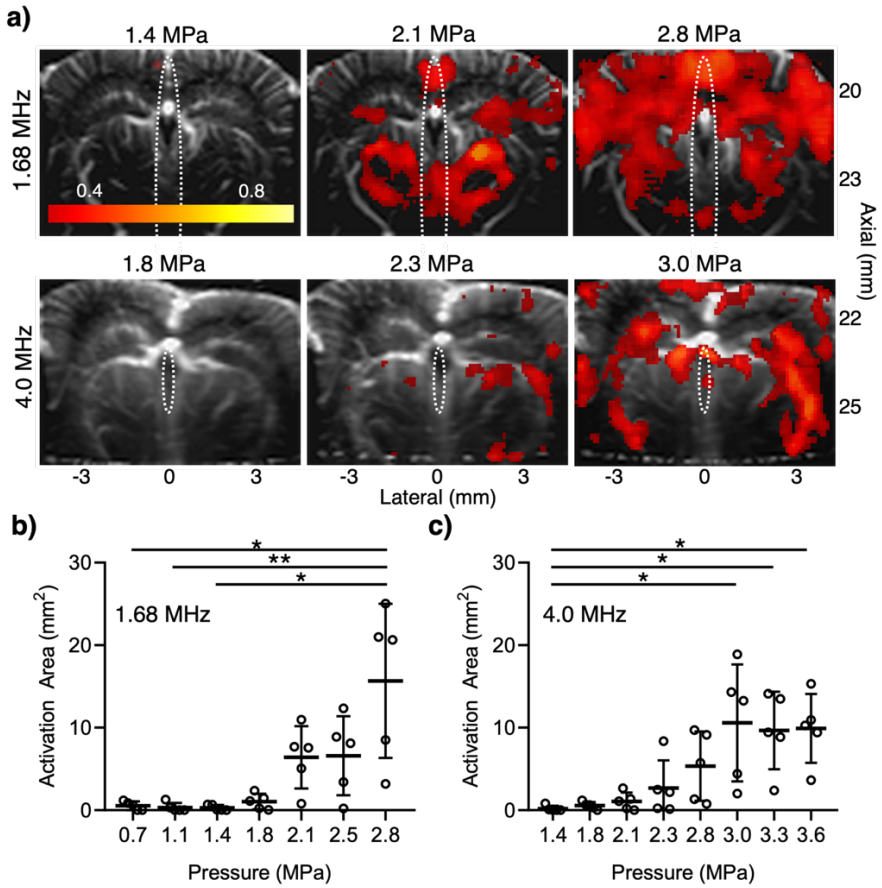

Figure 8. Higher pressures with different center frequencies induce greater activation in craniotomized mice. **(a)** Representative activity maps for 2 subjects receiving FUS with 1.68 MHz or 4.0 MHz center frequency under different pressure conditions. The predicted acoustic focus (white) assessed during transducer calibration is overlaid onto the PDIs. The color bar represents Spearman correlation values. **(b)** Activation area for different pressures in the 1.68 MHz condition. **(c)** Activation area for different pressures in the 4.0 MHz condition. Data is depicted as individual observations (circles) with mean (central line) and standard deviations (whiskers). (* $p < 0.05$; ** $p < 0.01$)

A separate experiment investigated whether unilateral targeting of FUS in a single hemisphere produces lateralized responses. FUS was targeted 2 mm left and right of the midline in each imaging plane in 13 paired trials across 6 subjects. Unilateral sonications produced bilateral hemodynamic responses with subcortical activation observed in most subjects. Significantly greater activation areas were observed ipsilateral to the sonicated hemisphere (Figure 9, $p < 0.01$). The overall success rate of activation across unilateral sonication trials was 80% ($n = 26$). Focally aligning activation area maps across these trials revealed a mean centroid distance of -0.031±0.216 mm from the focal axis.

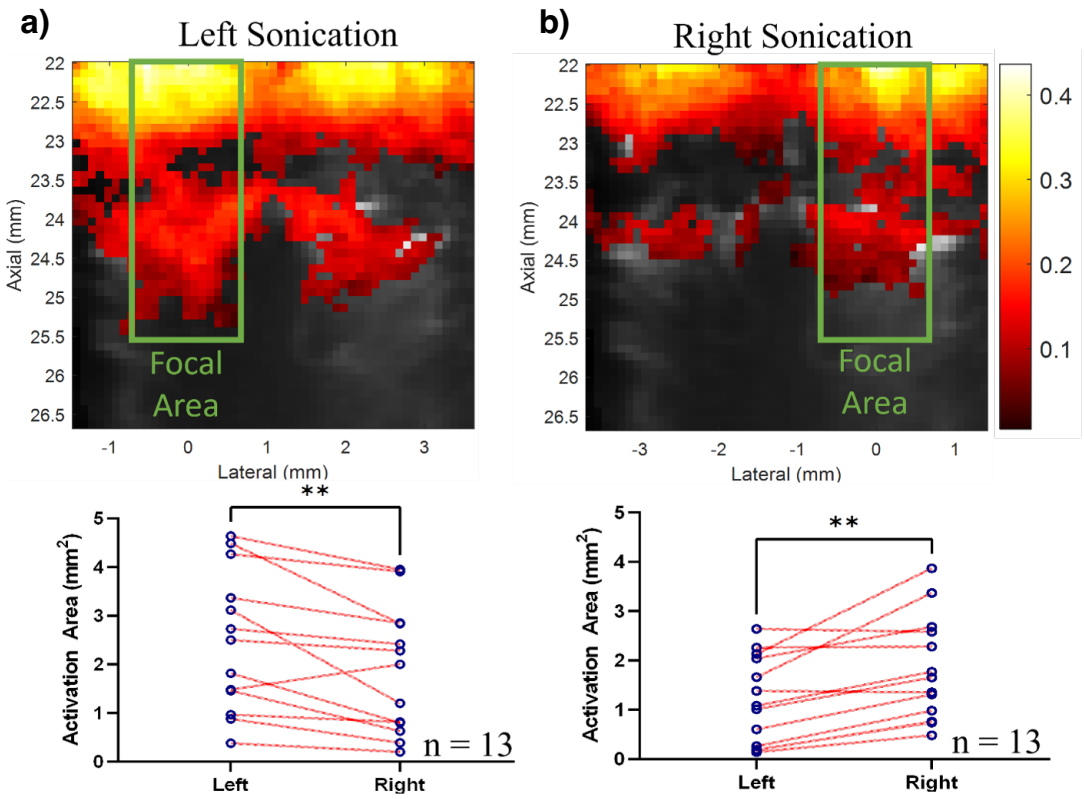

Figure 9. Ipsilateral bias in unilateral sonications. A total of 13 paired trials of unilateral sonications were performed across 6 subjects. Activation maps (Spearman correlation, $p < 0.01$) were averaged for **(a)** left and **(b)** right hemispheric sonications. Paired t-tests for activation area size in the left- versus right-hand halves of the imaging planes were performed for each paired set of unilateral sonications. Activation areas were significantly greater in the sonicated hemisphere (** $p < 0.01$).

A best-case example for focal activation is provided in Figure 10 showing three ROIs and their averaged CBV responses over time. This subject was sonicated at the midline (0 mm ML). Although bilateral activity was observed, there is a stretch of activity that extends into the subcortical region along the focal axis.

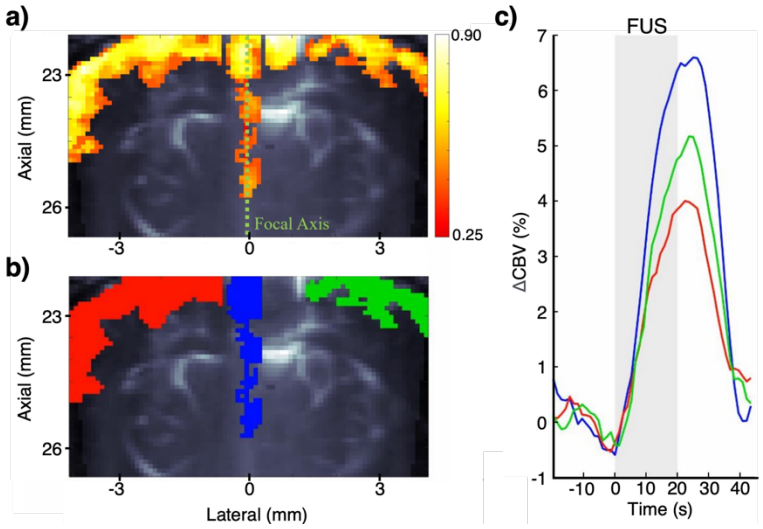

Figure 10. Example of CBV changes over time in one mouse induced by FUS neuromodulation. **(a)** The activity map produced by FUS neuromodulation (Spearman correlation, Pixels with $p < 0.01$). **(b)** Three regions of interest extracted from the activity map are labeled by color. **(c)** The CBV changes over time associated with each of the three regions are plotted according to the color of the region in **(b)**. FUS was applied at 0 mm laterally as indicated by the dotted green line in **(a)**.

Non-human primates

We translated our experimental setup from mice to NHP by making use of lower center frequencies for FUS neuromodulation and fUSI (Table 1). A total of 4 experiments in 2 subjects were performed to demonstrate the feasibility of our approach. Supplementary Figure 2 shows an example of activity maps for 6 individual neuromodulation trials (1 experiment) overlaid onto B-Mode images with traces of cerebral blood volume (CBV) change. For further analysis, the six trials from each experiment were averaged to improve the signal-to-noise ratio. We found significantly activated areas in all four experiments that were mainly localized to the center of the image where the focus is predicted to be and in cortical areas (Figure 11). Surprisingly we were also able to identify negatively correlated areas that showed decreases in CBV during and following FUS neuromodulation. However, negative changes in CBV were less pronounced than positive CBV changes across all subjects (Figure 11, Maximum CBV decrease: 2.5 % - 9.6 %; Maximum CBV increase: 10.0 % - 46.0 %). The average size of the activated area following sonications of 4 separate targets across both subjects was 56.9 ± 26.5 mm^2 and 40.3 ± 18.0 mm^2 for the positively and negatively correlated areas, respectively. The subsequent BBBO procedure and contrast-enhanced MRI in the same region as the neuromodulation session revealed successful delivery of acoustic energy to deep brain regions in all four experiments (Suppl. Figure 3).

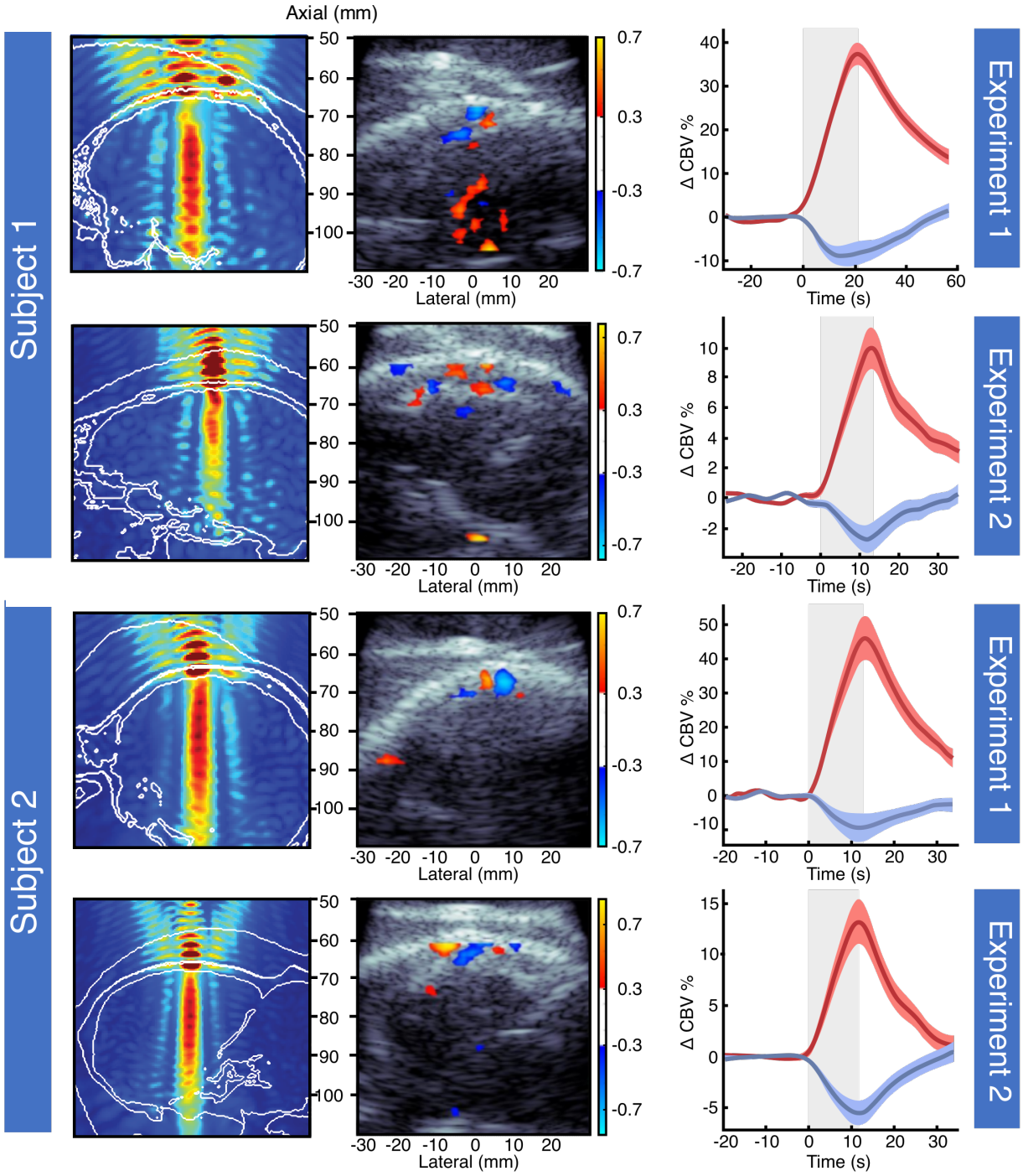

Figure 11. FUS targets and corresponding fUSI activity maps and CBV changes in NHP. Each row represents an experiment with n = 6 stimulus sessions that were averaged for further analysis. The first column shows simulation results, the second column shows activity maps (Spearman correlation) and the third column CBV changes in the significantly correlated areas (red: positive correlation, blue: negative correlation, shaded area: 95 % confidence interval). The fUSI transducer was aligned in the coronal plane or sagittal plane in experiments 1 and 2, respectively.

Discussion

This study presents the first implementation of transcranial fUSI in combination with FUS to investigate neuromodulatory effects in the CNS by analyzing changes in CBV. We demonstrate that higher pressures significantly increase the activated area in the brain and induce stronger CBV increases, while lateralized sonications result in CBV responses with ipsilateral bias in mice. Finally, we show the feasibility of our approach in NHPs, establishing the first successful implementation of transcranial fUSI in a large animal model.

Our results show robust and repeatable bilateral activation of cortical and subcortical areas during FUS neuromodulation not strictly limited to the focal area. This finding is seemingly in contrast with several studies demonstrating focal activation and specific behavioral responses during or following FUS[2,5,46–48]. However, others have demonstrated off-target activations likely associated with brain regions connected to the same network as the targeted areas[49] and network-associated changes in functional connectivity following FUS neuromodulation are widely reported[50–53]. The long neuromodulation periods (20 s) and high pressures (up to 3.6 MPa) employed in this study make it conceivable that connected brain areas were activated, while the comparatively low frame rate of fUSI (1-2 Hz) did not allow the identification of a focal starting point. This notion is partially supported by the facts that the induced CBV responses remained consistent at single transducer positions, that a smaller focus induced less activation and that lateral sonications produced an ipsilateral bias in the activated areas. Further studies that combine fUSI with electrical or optical recordings of neuronal activity in multiple brain regions are needed to fully elucidate the short-term activation patterns generated by FUS neuromodulation in the brain.

Subcortical activation was inconsistent during transcranial fUSI acquisitions while reliable activation was observed in the cortex. In mice implanted with an ultrasound-transparent cranial window, we found more robust activation in subcortical regions and less pronounced cortical activation, while the correlation with the stimulus vector appeared weaker in general. These results could be explained by the effects of temperature on neuronal activation since the brain temperature was decreased in mice with a cranial window, especially in cortical areas. Thermocouple measurements revealed a temperature of 31.6 °C in the cortex and 33.6 °C in the thalamus in the cranial window condition (Supplementary Figure 4), whereas brain temperature under similar anesthetic conditions without a cranial window has been reported by others to be 34.6 °C or 35.4

°C, respectively[54]. In addition, FUS can cause skull heating due to the acoustic properties of the skull, which results in a local temperature increase below the skull surface[55,56]. It has been shown repeatedly that temperature can influence neuronal activation and cerebral blood flow[57–60]. Specifically, temperature decreases induce lower cerebral blood flow, while the effects on neuronal activity are mostly described as excitatory[57,59]. Both mechanisms as well as skull heating likely influence the results presented here and could explain the differences between the activation profiles in the transcranial and cranial window conditions. Furthermore, lower temperature decreases the activity of mechanosensitive channels like Piezo1[61] and TRPP2[62] which have been shown to excite neurons during FUS neuromodulation[63]. Further investigation of the effects of temperature in the context of fUSI and during FUS neuromodulation is therefore warranted to advance our understanding and refine the application of both techniques. In addition, the stronger cortical activation and less pronounced subcortical response in the transcranial condition compared to animals with a cranial window should caution authors to directly translate results between both cases and carefully adjust relevant parameters like the cranial temperature.

We tested the feasibility of an adapted version of our FUS-fUSI setup in NHPs and were able to show robust responses to FUS neuromodulation. The activity maps following FUS neuromodulation were similar to the ones obtained transcranially in mice in the sense that all of them displayed cortical activation. In one case, activation maps matched the predicted focal area of neuromodulation very well. The differences in results could be explained by individual differences in skull properties that might affect fUSI and by small errors in the targeting procedure[64,65]. Interestingly, we were able to identify negatively correlated regions with stimulation-associated decreases in CBV, which could be connected to decreases in neuronal activity[66]. However, a variety of different mechanisms like a 'steal-phenomenon'[67] in the vicinity of active regions or vasoconstriction independent of neuronal activity[68] have been proposed. To allow translation from mice to NHPs the setup was adjusted by lowering the frequency of the FUS transducer and the fUSI array and increasing the number of compounded frames for PDI. These adjustments decrease temporal as well as spatial resolution and further studies are necessary to fully understand the limits of our method. Technical improvements like coded excitation might be able to increase SNR without sacrificing resolution in the future[69,70]. The high increase in CBV in NHPs were in contrast to our results in rodents, but are within the range of what others have reported with visual stimulation or in task-related behavioral paradigms[34,35]. Interestingly, we

found stronger increases in CBV while imaging in the coronal plane although the sagittal plane resulted in greater normality of the skull along the transducer surface that should have increased the gain of the functional signal. Additional studies are warranted to fully understand the effects of different imaging planes and skull aberrations on the quality of transcranial fUSI. Including greater or lesser portions of the skull should also affect the cutoff threshold of SVD filtering since a larger skull piece in the field of view would manifest as greater energy in the lower singular values. The effect of SVD cutoff value on the quality of fUSI data therefore requires further examination. Additional studies will need to be performed at identical targets across multiple independent experimental days to validate the repeatability of FUS-evoked fUSI responses in NHPs.

Conclusion

This study introduced a system for FUS neuromodulation that allows simultaneous online monitoring of hemodynamic responses with fUSI *in vivo*. We show that fUSI can capture region-dependent responses to FUS neuromodulation and displays stronger responses in higher-pressure conditions. Our approach allowed for transcranial imaging of FUS neuromodulation-induced changes with a large field of view in rodents, which could help in studying the immediate to mid-term effects of FUS neuromodulation, especially in the context of network activation patterns. Finally, this study demonstrated for the first time that transcranial fUSI can detect FUS neuromodulation-evoked hemodynamic changes in nonhuman primates. Although results need to be validated in different brain regions and with a larger number of subjects, the findings presented herein could serve as a framework for implementing fully non-invasive FUS neuromodulation with simultaneous indirect monitoring of neuronal activity in humans.

Declaration of competing interest

The authors declare that they have no known competing financial interests or personal relationships that could have appeared to influence the work reported in this paper.

Acknowledgments

This work was supported by the National Institutes of Health (Award numbers: 5R01EB02757 6-04 and 5R01AG03896 1-10) and Jonas Bendig was partially supported by the Thiemann Foundation. Additionally, we would like to thank Dr. Stephen Lee for his crucial advice and support during the whole project.

References

1. Hameroff, S. *et al.* Transcranial ultrasound (TUS) effects on mental states: a pilot study. *Brain Stimulat.* **6**, 409–415 (2013).
2. Tufail, Y. *et al.* Transcranial pulsed ultrasound stimulates intact brain circuits. *Neuron* **66**, 681–694 (2010).
3. Tufail, Y., Yoshihiro, A., Pati, S., Li, M. M. & Tyler, W. J. Ultrasonic neuromodulation by brain stimulation with transcranial ultrasound. *Nat. Protoc.* **6**, 1453–1470 (2011).
4. Murphy, K. R. *et al.* A tool for monitoring cell type-specific focused ultrasound neuromodulation and control of chronic epilepsy. *Proc. Natl. Acad. Sci. U. S. A.* **119**, e2206828119 (2022).
5. Yoo, S.-S. *et al.* Focused ultrasound modulates region-specific brain activity. *Neuroimage* **56**, 1267–1275 (2011).
6. Yu, K., Niu, X., Krook-Magnuson, E. & He, B. Intrinsic functional neuron-type selectivity of transcranial focused ultrasound neuromodulation. *Nat. Commun.* **12**, 2519 (2021).
7. Fry, F. J., Ades, H. W. & Fry, W. J. Production of reversible changes in the central nervous system by ultrasound. *Science* **127**, 83–84 (1958).
8. Sarica, C. *et al.* Human Studies of Transcranial Ultrasound neuromodulation: A systematic review of effectiveness and safety. *Brain Stimulat.* **15**, 737–746 (2022).
9. Kamimura, H. A. S., Conti, A., Toschi, N. & Konofagou, E. E. Ultrasound neuromodulation: mechanisms and the potential of multimodal stimulation for neuronal function assessment. *Front. Phys.* **8**, 150 (2020).
10. Fomenko, A., Neudorfer, C., Dallapiazza, R. F., Kalia, S. K. & Lozano, A. M. Low-intensity ultrasound neuromodulation: An overview of mechanisms and emerging human applications. *Brain Stimulat.* **11**, 1209–1217 (2018).

11. Aurup, C., Kamimura, H. A. S. & Konofagou, E. E. High-Resolution Focused Ultrasound Neuromodulation Induces Limb-Specific Motor Responses in Mice in Vivo. *Ultrasound Med. Biol.* **47**, 998–1013 (2021).
12. Hernandez-Pavon, J. C. *et al.* TMS combined with EEG: Recommendations and open issues for data collection and analysis. *Brain Stimul. Basic Transl. Clin. Res. Neuromodulation* **16**, 567–593 (2023).
13. Chen, S., Mohajerani, M. H., Xie, Y. & Murphy, T. H. Optogenetic analysis of neuronal excitability during global ischemia reveals selective deficits in sensory processing following reperfusion in mouse cortex. *J. Neurosci. Off. J. Soc. Neurosci.* **32**, 13510–13519 (2012).
14. Ahrens, E. T. & Dubowitz, D. J. Peripheral somatosensory fMRI in mouse at 11.7 T. *NMR Biomed.* **14**, 318–324 (2001).
15. Bosshard, S. C. *et al.* Assessment of brain responses to innocuous and noxious electrical forepaw stimulation in mice using BOLD fMRI. *Pain* **151**, 655–663 (2010).
16. Deffieux, T., Demene, C., Pernot, M. & Tanter, M. Functional ultrasound neuroimaging: a review of the preclinical and clinical state of the art. *Curr. Opin. Neurobiol.* **50**, 128–135 (2018).
17. Martinez de Paz, J. M. & Macé, E. Functional ultrasound imaging: A useful tool for functional connectomics? *NeuroImage* **245**, 118722 (2021).
18. Montaldo, G., Urban, A. & Macé, E. Functional Ultrasound Neuroimaging. *Annu. Rev. Neurosci.* **45**, 491–513 (2022).
19. Urban, A. *et al.* Real-time imaging of brain activity in freely moving rats using functional ultrasound. *Nat. Methods* **12**, 873–878 (2015).
20. Brunner, C. *et al.* Whole-brain functional ultrasound imaging in awake head-fixed mice. *Nat. Protoc.* **16**, 3547–3571 (2021).
21. Macé, E. *et al.* Functional ultrasound imaging of the brain. *Nat. Methods* **8**, 662–664 (2011).
22. Ionescu, T. M., Grohs-Metz, G. & Hengerer, B. Functional ultrasound detects frequency-specific acute and delayed S-ketamine effects in the healthy mouse brain. *Front. Neurosci.* **17**, 1177428 (2023).
23. Rabut, C. *et al.* Pharmaco-fUS: Quantification of pharmacologically-induced dynamic changes in brain perfusion and connectivity by functional ultrasound imaging in awake mice. *NeuroImage* **222**, 117231 (2020).
24. Rabut, C. *et al.* 4D functional ultrasound imaging of whole-brain activity in rodents. *Nat. Methods* **16**, 994–997 (2019).
25. Osmanski, B.-F., Pezet, S., Ricobaraza, A., Lenkei, Z. & Tanter, M. Functional ultrasound imaging of intrinsic connectivity in the living rat brain with high spatiotemporal resolution. *Nat. Commun.* **5**, 5023 (2014).
26. Baranger, J. *et al.* Adaptive Spatiotemporal SVD Clutter Filtering for Ultrafast Doppler Imaging Using Similarity of Spatial Singular Vectors. *IEEE Trans. Med. Imaging* **37**, 1574–1586 (2018).
27. Demené, C. *et al.* Spatiotemporal Clutter Filtering of Ultrafast Ultrasound Data Highly Increases Doppler and fUltrasound Sensitivity. *IEEE Trans. Med. Imaging* **34**, 2271–2285 (2015).
28. Claron, J. *et al.* Co-variations of cerebral blood volume and single neurons discharge during resting state and visual cognitive tasks in non-human primates. *Cell Rep.* **42**, 112369 (2023).
29. Nunez-Elizalde, A. O. *et al.* Neural correlates of blood flow measured by ultrasound. *Neuron* **110**, 1631-1640.e4 (2022).

30. Mace, E. *et al.* Functional ultrasound imaging of the brain: theory and basic principles. *IEEE Trans. Ultrason. Ferroelectr. Freq. Control* **60**, 492–506 (2013).
31. Aurup, C., Pouliopoulos, A. N., Kwon, N., Murillo, M. F. & Konofagou, E. E. Evaluation of Non-invasive Optogenetic Stimulation with Transcranial Functional Ultrasound Imaging. *Ultrasound Med. Biol.* **49**, 908–917 (2023).
32. Bertolo, A. *et al.* Whole-Brain 3D Activation and Functional Connectivity Mapping in Mice using Transcranial Functional Ultrasound Imaging. *J. Vis. Exp. JoVE* (2021) doi:10.3791/62267.
33. Tiran, E. *et al.* Transcranial Functional Ultrasound Imaging in Freely Moving Awake Mice and Anesthetized Young Rats without Contrast Agent. *Ultrasound Med. Biol.* **43**, 1679–1689 (2017).
34. Blaize, K. *et al.* Functional ultrasound imaging of deep visual cortex in awake nonhuman primates. *Proc. Natl. Acad. Sci.* **117**, 14453–14463 (2020).
35. Dizeux, A. *et al.* Functional ultrasound imaging of the brain reveals propagation of task-related brain activity in behaving primates. *Nat. Commun.* **10**, 1400 (2019).
36. Griggs, W. S. *et al.* Decoding motor plans using a closed-loop ultrasonic brain–machine interface. *Nat. Neurosci.* **27**, 196–207 (2024).
37. Norman, S. L. *et al.* Single Trial Decoding of Movement Intentions Using Functional Ultrasound Neuroimaging. *Neuron* **109**, 1554-1566.e4 (2021).
38. Bae, S., Liu, K., Pouliopoulos, A. N., Ji, R. & Konofagou, E. E. Real-Time Passive Acoustic Mapping With Enhanced Spatial Resolution in Neuronavigation-Guided Focused Ultrasound for Blood-Brain Barrier Opening. *IEEE Trans. Biomed. Eng.* **70**, 2874–2885 (2023).
39. Sato, T., Shapiro, M. G. & Tsao, D. Y. Ultrasonic Neuromodulation Causes Widespread Cortical Activation via an Indirect Auditory Mechanism. *Neuron* **98**, 1031-1041.e5 (2018).
40. Guo, H. *et al.* Ultrasound Produces Extensive Brain Activation via a Cochlear Pathway. *Neuron* **98**, 1020-1030.e4 (2018).
41. Mohammadjavadi, M. *et al.* Elimination of peripheral auditory pathway activation does not affect motor responses from ultrasound neuromodulation. *Brain Stimulat.* **12**, 901–910 (2019).
42. Paxinos, G. & Franklin, K. *Paxinos and Franklin's the Mouse Brain in Stereotaxic Coordinates*. (Elsevier Academic Press, 2019).
43. Wu, S.-Y. *et al.* Efficient Blood-Brain Barrier Opening in Primates with Neuronavigation-Guided Ultrasound and Real-Time Acoustic Mapping. *Sci. Rep.* **8**, 7978 (2018).
44. Pouliopoulos, A. N. *et al.* Safety evaluation of a clinical focused ultrasound system for neuronavigation guided blood-brain barrier opening in non-human primates. *Sci. Rep.* **11**, 15043 (2021).
45. Treeby, B. E. & Cox, B. T. k-Wave: MATLAB toolbox for the simulation and reconstruction of photoacoustic wave fields. *J. Biomed. Opt.* **15**, 021314 (2010).
46. Kamimura, H. A. S. *et al.* Focused ultrasound neuromodulation of cortical and subcortical brain structures using 1.9 MHz. *Med. Phys.* **43**, 5730 (2016).
47. Yang, Y. *et al.* Induction of a torpor-like hypothermic and hypometabolic state in rodents by ultrasound. *Nat. Metab.* **5**, 789–803 (2023).
48. Ai, L., Bansal, P., Mueller, J. K. & Legon, W. Effects of transcranial focused ultrasound on human primary motor cortex using 7T fMRI: a pilot study. *BMC Neurosci.* **19**, 56 (2018).
49. Yang, P.-F. *et al.* Bidirectional and state-dependent modulation of brain activity by transcranial focused ultrasound in non-human primates. *Brain Stimulat.* **14**, 261–272 (2021).

50. Yaakub, S. N. *et al.* Transcranial focused ultrasound-mediated neurochemical and functional connectivity changes in deep cortical regions in humans. *Nat. Commun.* **14**, 5318 (2023).
51. Folloni, D. *et al.* Manipulation of Subcortical and Deep Cortical Activity in the Primate Brain Using Transcranial Focused Ultrasound Stimulation. *Neuron* **101**, 1109-1116.e5 (2019).
52. Verhagen, L. *et al.* Offline impact of transcranial focused ultrasound on cortical activation in primates. *eLife* **8**, e40541 (2019).
53. Sanguinetti, J. L. *et al.* Transcranial Focused Ultrasound to the Right Prefrontal Cortex Improves Mood and Alters Functional Connectivity in Humans. *Front. Hum. Neurosci.* **14**, 52 (2020).
54. Shirey, M. J. *et al.* Brief anesthesia, but not voluntary locomotion, significantly alters cortical temperature. *J. Neurophysiol.* **114**, 309–322 (2015).
55. Kim, C. *et al.* Closed-loop trans-skull ultrasound hyperthermia leads to improved drug delivery from thermosensitive drugs and promotes changes in vascular transport dynamics in brain tumors. *Theranostics* **11**, 7276–7293 (2021).
56. Blackmore, D. G. *et al.* Low-intensity ultrasound restores long-term potentiation and memory in senescent mice through pleiotropic mechanisms including NMDAR signaling. *Mol. Psychiatry* **26**, 6975–6991 (2021).
57. Kim, T. *et al.* Thermal effects on neurons during stimulation of the brain. *J. Neural Eng.* **19**, 056029 (2022).
58. Kiyatkin, E. A. Brain temperature and its role in physiology and pathophysiology: Lessons from 20 years of thermorecording. *Temp. Multidiscip. Biomed. J.* **6**, 271–333 (2019).
59. Van Hook, M. J. Temperature effects on synaptic transmission and neuronal function in the visual thalamus. *PLoS ONE* **15**, e0232451 (2020).
60. Wang, H. *et al.* Brain temperature and its fundamental properties: a review for clinical neuroscientists. *Front. Neurosci.* **8**, (2014).
61. Zheng, W., Nikolaev, Y. A., Gracheva, E. O. & Bagriantsev, S. N. Piezo2 integrates mechanical and thermal cues in vertebrate mechanoreceptors. *Proc. Natl. Acad. Sci. U. S. A.* **116**, 17547–17555 (2019).
62. Ng, L. C. T., Vien, T. N., Yarov-Yarovoy, V. & DeCaen, P. G. Opening TRPP2 (PKD2L1) requires the transfer of gating charges. *Proc. Natl. Acad. Sci. U. S. A.* **116**, 15540–15549 (2019).
63. Yoo, S., Mittelstein, D. R., Hurt, R. C., Lacroix, J. & Shapiro, M. G. Focused ultrasound excites cortical neurons via mechanosensitive calcium accumulation and ion channel amplification. *Nat. Commun.* **13**, 493 (2022).
64. Pouliopoulos, A. N. *et al.* A clinical system for non-invasive blood-brain barrier opening using a neuronavigation-guided single-element focused ultrasound transducer. *Ultrasound Med. Biol.* **46**, 73–89 (2020).
65. Bae, S. *et al.* Transcranial Blood-Brain Barrier Opening in Alzheimer's Disease Patients Using A Portable Focused Ultrasound System with Real-Time 2-D Cavitation Mapping. *MedRxiv Prepr. Serv. Health Sci.* 2023.12.21.23300222 (2024) doi:10.1101/2023.12.21.23300222.
66. Macé, É. *et al.* Whole-Brain Functional Ultrasound Imaging Reveals Brain Modules for Visuomotor Integration. *Neuron* **100**, 1241-1251.e7 (2018).
67. Harel, N., Lee, S.-P., Nagaoka, T., Kim, D.-S. & Kim, S.-G. Origin of negative blood oxygenation level-dependent fMRI signals. *J. Cereb. Blood Flow Metab. Off. J. Int. Soc. Cereb. Blood Flow Metab.* **22**, 908–917 (2002).

68. Shih, Y.-Y. I. *et al.* A new scenario for negative functional magnetic resonance imaging signals: endogenous neurotransmission. *J. Neurosci. Off. J. Soc. Neurosci.* **29**, 3036–3044 (2009).
69. Vienneau, E. P. & Byram, B. C. A Coded Excitation Framework for High SNR Transcranial Ultrasound Imaging. *IEEE Trans. Med. Imaging* **42**, 2886–2898 (2023).
70. Vienneau, E., Weeks, A. & Byram, B. Coded Excitation for Increased Sensitivity in Transcranial Power Doppler Imaging. in *2022 IEEE International Ultrasonics Symposium (IUS)* 1–4 (2022). doi:10.1109/IUS54386.2022.9958842.